Chemical Science

ROYAL SOCIETY OF CHEMISTRY

EDGE ARTICLE

View Article Online
View Journal | View Issue

Cite this: *Chem. Sci.*, 2023, **14**, 5906

All publication charges for this article have been paid for by the Royal Society of Chemistry

Received 23rd December 2022
Accepted 2nd May 2023

DOI: 10.1039/d2sc07034k

rsc.li/chemical-science

Direct observation of the dynamic reconstructed active phase of perovskite $LaNiO_3$ for the oxygen-evolution reaction†

Yan Sun,[a] Cheng-Rong Wu,[a] Tian-Yi Ding,[a] Jian Gu,[a] Jia-Wei Yan, *[a] Jun Cheng *[ab] and Kelvin H. L. Zhang *[ab]

Ni-based transition metal oxides are promising oxygen-evolution reaction (OER) catalysts due to their abundance and high activity. Identification and manipulation of the chemical properties of the real active phase on the catalyst surface is crucial to improve the reaction kinetics and efficiency of the OER. Herein, we used electrochemical-scanning tunnelling microscopy (EC-STM) to directly observe structural dynamics during the OER on $LaNiO_3$ (LNO) epitaxial thin films. Based on comparison of dynamic topographical changes in different compositions of LNO surface termination, we propose that reconstruction of surface morphology originated from transition of Ni species on LNO surface termination during the OER. Furthermore, we showed that the change in surface topography of LNO was induced by $Ni(OH)_2$/NiOOH redox transformation by quantifying STM images. Our findings demonstrate that *in situ* characterization for visualization and quantification of thin films is very important for revealing the dynamic nature of the interface of catalysts under electrochemical conditions. This strategy is crucial for in-depth understanding of the intrinsic catalytic mechanism of the OER and rational design of high-efficiency electrocatalysts.

Electrochemical water-splitting is a promising technology for storage of renewable energy.[1–3] However, widespread application is hampered by the sluggish kinetics of the oxygen-evolution reaction (OER), which is reliant on rare and expensive noble metal oxides (*e.g.*, Ir-based oxides).[4] Thus, earth–abundant transition metal oxides (transition metal = Co, Ni and Fe) have attracted much attention due to their low cost and high activity in alkaline conditions.[5–11] To design highly active and stable catalysts, chemists have made tremendous endeavours to investigate the structure of active phases under OER conditions and elucidate how the reconstructed structures accelerate reactions. Recent works show that the formation of a new active surface can be triggered by defect conformation,[12,13] doping with metal elements[14–17] and leaching anions or cations.[18] With the advent of *in situ*/operando microscopic and spectroscopic methods (*e.g.*, X-ray absorption fine structure,[19] Raman,[20] Fourier transform infrared,[21] X-ray diffraction (XRD)[22] and UV-visible absorption (UV-vis)),[23] identification of the dynamic perspective of active phases instead of static phases has attracted much interest in recent studies.

However, most of those works have relied on nanostructured catalysts with different surface areas and morphologies. It is difficult to describe the structure–activity relationship accurately owing to disordered structures.[24,25] Epitaxial oxide single-crystal thin films can address this issue due to their atomically flat surfaces and tightly controlled compositions.[26,27] It has been demonstrated that such films can serve as an ideal platform to explore intrinsic activities and electronic properties for in-depth mechanistic studies.

The catalyst surface or catalyst–electrolyte interface is the place where chemical reactions occur, and they usually have different properties from the corresponding bulk materials.[28–30] Understanding the structure–activity relationship on the surface or interface is of great importance to optimize or design catalysts, and can be investigated using electrochemical scanning tunnelling microscopy (EC-STM). EC-STM is particularly well suited to the study of flat films because it can provide structural information with high resolution directly under reaction control.[31,32] Very few oxide electrocatalysts have been explored by EC-STM. For example, Stumm *et al.*[33] reported the surface dynamics of CoO_x nano islands on Au (111) during the OER. However, that model catalytic system was affected by the substrate, which hampered analyses of morphological changes. Hence, an oxide single-crystal thin film is suitable to explore

[a]*State Key Laboratory of Physical Chemistry of Solid Surfaces, iChEM, College of Chemistry and Chemical Engineering, Xiamen University, Xiamen 361005, China. E-mail: jwyan@xmu.edu.cn; chengjun@xmu.edu.cn; kelvinzhang@xmu.edu.cn*

[b]*Innovation Laboratory for Sciences and Technologies of Energy Materials of Fujian Province (IKKEM), Xiamen 361005, China*

† Electronic supplementary information (ESI) available. See DOI: https://doi.org/10.1039/d2sc07034k

surface effects under reaction conditions. EC-STM investigations on a thin-film catalyst are lacking.

Herein, by combining oxide single-crystal thin films grown by pulsed laser deposition (PLD) and EC-STM (Fig. 1a), we provide direct observation of dynamic surface reconstruction on a single crystal surface during the OER. We used perovskite $LaNiO_3$ (LNO) as a model catalyst, which has attracted considerable attention due to its high efficiency and low cost.[34] The performance of LNO has been studied deeply (*e.g.*, effect of chemical substitution[35–39] and role of lattice oxygen during the OER).[40] Based on the layered structure of LNO, we tuned the composition of surface termination by controlling film-growth conditions. In this way, we investigated the relationship between the termination composition and restructuring properties of the surface during the OER. Then, we undertook quantitative analyses of EC-STM images to reveal the structural evolution of the oxide layer on Ni-rich and La-rich terminated surfaces under the OER. We found that surface restructuring originated from the formation of a newly active Ni-oxyhydroxide-type layer which was correlated directly to the redox potential. Also, this new active layer further was reconfigured during the OER, which was reversible with respect to the applied potential. Our work showcases an EC-STM-based method to directly observe transformation of the dynamic active phase under reaction conditions. Our method could be used to identify the specific effect of a surface factor on the properties of electrocatalysts for the OER.

A perovskite LNO single-crystal thin film of thickness ~35 nm was grown in an epitaxial manner on Nb-doped $SrTiO_3$ (001) (Nb-STO) using PLD. To tune the surface composition, we varied the growth temperature during LNO deposition. Ni-rich terminated and La-rich terminated LNO thin films were deposited at temperatures of 450 °C and 750 °C, respectively, which have been used successfully for study of the termination–activity relationship previously.[41] All films showed atomic flat terraces of width ~200 nm, as shown in atomic force microscopy (AFM) images (Fig. 1b and c). XRD spectroscopy confirmed the high quality of thin films with an epitaxial relationship of films (001) ǁ STO (001) (Fig. S1 in ESI†).

To determine a depth profile of chemical elements, we used angle-resolved X-ray photoelectron spectroscopy (ARXPS) which, in general, is an effective method to characterize surface termination.[42] ARXPS was used to compare peak area ratios for La to Ni in a bulk-sensitive configuration ($\theta = 0°$ in Fig. 2a) and a surface-sensitive configuration ($\theta = 60°$ in Fig. 2a). Ni 2p overlaps heavily with La 3d, so we chose core levels of La 4d and Ni 3p to further confirm surface termination.[43] The ARXPS spectra of the core levels of La 4d and Ni 3p were obtained by tilting samples at $\theta = 0°$ and $\theta = 60°$ for Ni-rich and La-rich terminated films, respectively (Fig. 2b and c). After normalization of bulk- and surface-sensitive La 4d and Ni 3p, the Ni 3p peak showed the same total peak area for Ni-rich terminated LNO, which highlighted a smaller peak area for the surface-sensitive La 4d peak relative to its bulk counterpart (black dashed square in Fig. 2b). The ratio of the peak areas of La 4d to Ni 3p decreased from 4.89 to 4.51 for θ from 0° to 60° in the Ni-rich terminated sample. For the sample with La-rich termination, the peak area of surface-sensitive Ni 3p was smaller than that of the bulk property with the same La 4d peak area (black

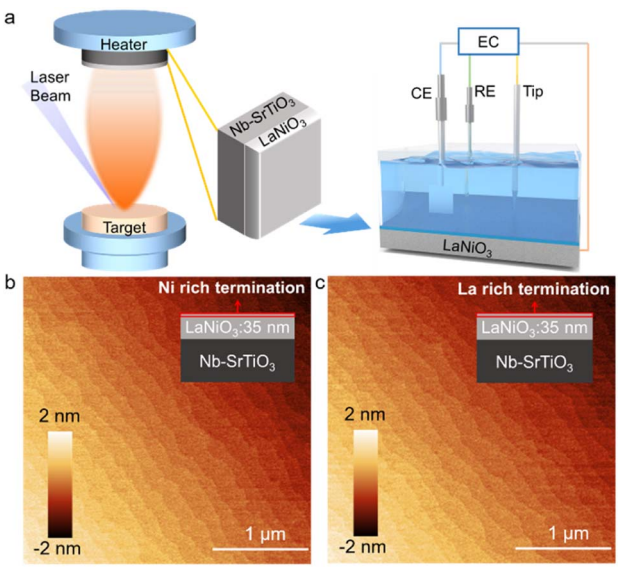

Fig. 1 (a) Growth of thin films and EC-STM (schematic). The left part is the working principle of PLD. $LaNiO_3$ epitaxial films were grown by PLD on Nb–$SrTiO_3$ substrates. EC-STM was carried out to investigate evolution of the surface structure during OER operations. The component of EC-STM is shown in the right part, and comprises a coated probe with an exposed tip, counter electrode, reference electrode, and working electrode of $LaNiO_3$ film. AFM images of Ni-rich terminated (b) and La-rich terminated (c) $LaNiO_3$ films with an area of 5 × 5 μm^2, showing atomically flat surfaces.

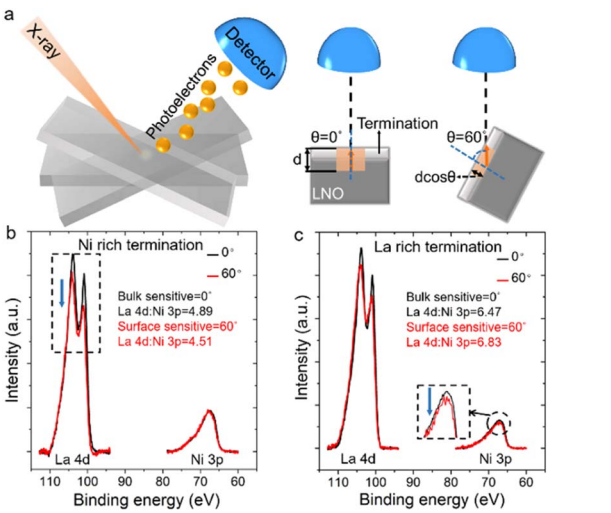

Fig. 2 (a) Principle of angle-resolved X-ray photoelectron spectroscopy (ARXPS) measurement. θ is the angle between the sample and detector column, and is controlled by tilting the sample stage. The sampling depth becomes $d\cos\theta$ with tilting of the sample. (b) La 4d and Ni 3p core-level spectra at $\theta = 0°$ and 60° for Ni-rich terminated LNO. (c) La 4d and Ni 3p core-level spectra at $\theta = 0°$ and 60° for La-rich terminated LNO.

dashed square in Fig. 2c). The ratio of the peak areas of La 4d to Ni 3p increased from 6.47 to 6.83 with decreasing sampling depth in the La-rich terminated sample.

In a next step, cyclic voltammetry (CV) of Ni- and La-rich terminated LNO was undertaken in alkaline solution (KOH solution at pH = 13). Fig. 3a and 4a show CV curves for the OER under a potential window from 1.12 V to 1.72 V. The potentials used were relative to the reversible hydrogen electrode (RHE) with *iR* correction ($E - iR$). The cyclic voltammogram for Ni termination exhibited one pair of redox peaks before onset of the OER, which was between 1.15 V and 1.4 V (inset image of Fig. 3a). This corresponded to a reduction/oxidation couple of Ni(II) and Ni(III), which is consistent with the literature.[41,44] These peaks disappeared in the cyclic voltammogram of La-rich terminated LNO (Fig. 4a), which further confirmed a Ni-lacking surface layer.

Then, we used EC-STM to systematically investigate the surface reconstruction by varying the applied potential. STM images were obtained under a constant potential of sample, and the acquisition time per image was ~2 min. The electrochemical cell was under a N_2 atmosphere to avoid the effect of CO_2 dissolution. Fig. 3b shows the surface morphology of Ni-rich terminated LNO with a mean height of 0.76 nm in KOH solution (pH = 13) at a potential more negative than the oxidation peak. In the literature,[5] most oxide catalysts have been used for the OER at a pH of 13–14, which is higher than the point of zero charge (pH_{pzc}) of most oxides (typically ranging from 7 to 11 for binary oxides and perovskites[45]). Hence, OH^- was expected to accumulate on the surface.[46] LNO (pH_{pzc} = 8.9)[45] was expected to be hydroxylated in a solution with a pH of 13. Furthermore, based on the Pourbaix diagram for a Ni-based

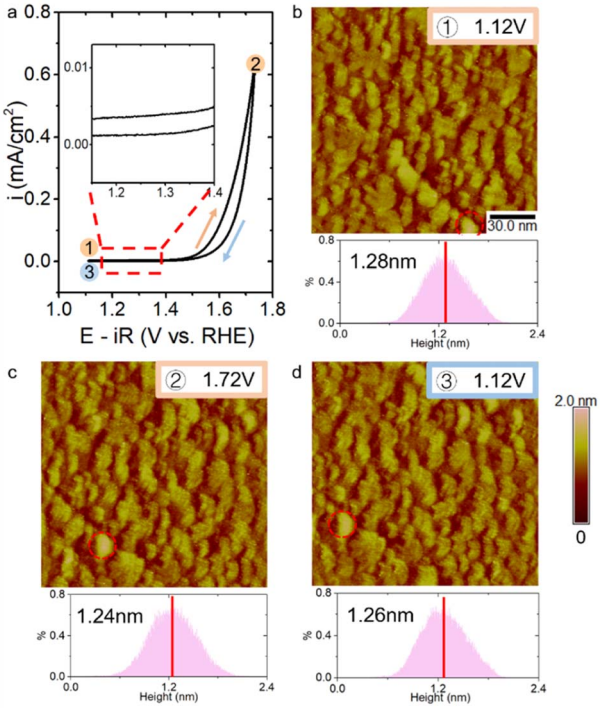

Fig. 4 (a) CV of La-rich terminated LNO with applied potentials at which the EC-STM images are obtained. The inset is an enlarged part of the cyclic voltammogram between 1.15 V to 1.4 V and the redox peaks are absent. EC-STM images were measured in the forward CV scan at (b) 1.12 V, (c) 1.72 V and a backward CV scan at (d) 1.12 V with a size of 150 × 150 nm^2. The lower pictures of b, c and d are the corresponding depth histograms of EC-STM images at different potentials.

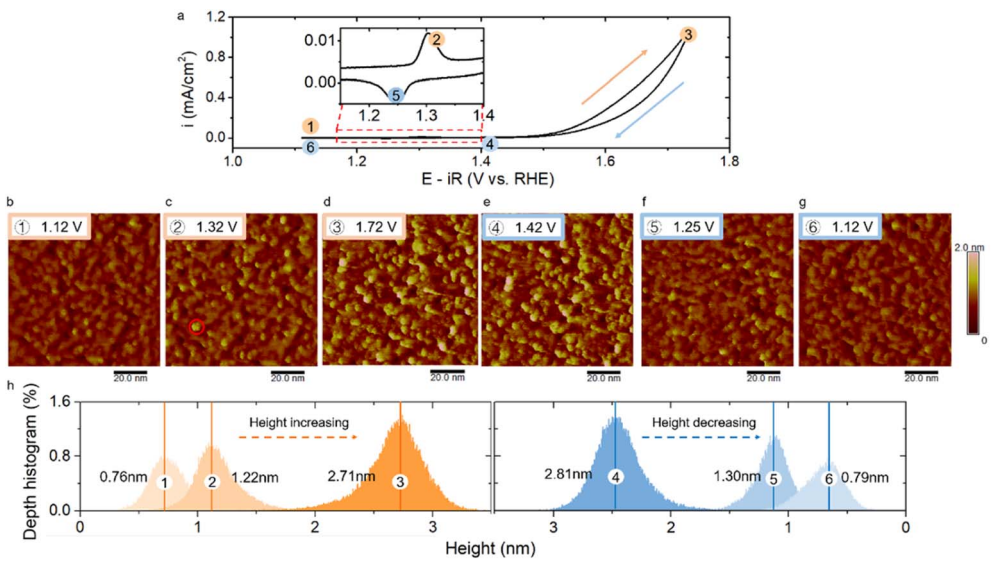

Fig. 3 (a) CV of Ni-rich terminated LNO with applied potentials at which EC-STM images were obtained. The inset is an enlarged part of cyclic voltammograms between 1.15 V to 1.4 V with one pair of redox peaks. EC-STM images measured in forward CV scans at applied potentials of (b) 1.12 V, (c) 1.32 V, (d) 1.72 V, and backward CV scans at (e) 1.42 V, (f) 1.25 V, and (g) 1.12 V with a size of 90 × 90 nm^2. (h) Depth histograms of EC-STM images at different potentials. The potential applied to the Pt/Ir tip was kept at 0.87 V, and all the potentials shown here were *versus* RHE. The tunnelling current was 1 nA.

oxide,[47] this hydroxylated structure would remain stable under the applied potential shown in Fig. 3b in a solution of pH = 13. Also, this topography, with several small clusters, was consistent with the hydroxylated surface reported by Liang *et al.*[48] They observed, by comparing the morphology under a vacuum and after exposure to water vapor in STM experiments, that the surface of NiO_x became rough and clusters arose during hydroxylation. Therefore, the topography observed in Fig. 3b should correspond to a hydroxylated surface under electrochemical conditions. To monitor the topographical changes as a function of applied potential, the Ni-rich terminated LNO was imaged by stepping the applied anodic and cathodic potentials. The evolution of morphologies with an increase in the applied potentials is shown in Fig. 3c and d. The LNO surface became rougher as the height of several particles increased (*e.g.*, the brighter particle shown in Fig. 3c in the red circle) at 1.32 V, which correlated with the oxidation reaction of Ni(II) to Ni(III). The transition with an increase in the cluster height continued at a higher applied potential. When the applied potential was increased to 1.72 V (Fig. 3d), the number and height of the brighter particles increased markedly with a vigorous OER (Fig. 3d). Furthermore, when the applied potential decreased, the surface roughness was almost unchanged (*e.g.*, 1.42 V in Fig. 3e). Then, when the applied potential was reduced to enable the reduction reaction of Ni(III) to Ni(II), the bright clusters disappeared (*e.g.*, 1.25 V in Fig. 3f). As the applied potential stepped back to the double-layer region before the reduction peak, the morphology returned to the original hydroxylated surface with a similar roughness to that shown in Fig. 3b. Based on the morphology changes observed, this surface reconstruction showed dynamic reversibility with respect to the applied potential. Also, we observed this reversible surface reconstruction over multiple CV cycles (Fig. S2†).

To quantify the surface reconstruction, we analysed the mean height and depth histograms of STM images. The reversible change in the surface morphology was reflected in a change in the mean height. The height distribution of the surface increased to a higher value when the Ni-related oxidation reaction occurred (Fig. 3h), and then increased rapidly with an enhanced OER. For instance, the mean height increased from 0.76 nm to 2.71 nm as the potential was stepped from 1.12 V to 1.72 V. This reversibility manifested in a reduction of the mean height when the potential decreased in the Ni-related reduction reaction. When the applied potential stepped back to the double-layer region, the height of the surface returned back to 0.79 nm, which is very close to the original height shown in Fig. 3b. This potential-dependent change in the mean surface height also illustrated the reversibility of surface reconstruction quantitatively.

We also explored the surface morphological changes of La-rich terminated LNO during the CV cycle by EC-STM. Ni-related redox peaks were absent on the La-rich surface. Surface changes could not be observed with an applied potential scanning forward and back between 1.12 V and 1.72 V. We labelled a particle with a special shape (red dotted circle in Fig. 4b–d) on the surface to ensure that the observed surface did not shift too far due to thermal disturbances. There was no change in the mean height and depth histograms of STM images during changes in the applied potential (lower pictures of Fig. 4b–d). These STM results clearly revealed potential-dependent surface reconstruction to be associated with a surface redox reaction of the Ni component.

Next, we mused on the possible origination of the surface transformation triggered by the applied potential. As reported by Baeumer *et al.*,[41] the origin of the surface Ni oxidation reaction could be a Ni oxyhydroxide-type phase formation. They demonstrated it by combining potential-dependent optical density (OD) changes in UV-vis spectroscopy for a LNO film with a 3 Å Ni rich-surface and density functional theory (DFT) calculations. Zhang *et al.*[49] also found the *in situ* Raman peaks corresponding to NiOOH appeared at an oxidation potential for Ni species on LNO nanomaterials. According to those studies, we could infer that the morphological change caused by the oxidation reaction around 1.3 V should be attributed to generation of the NiOOH phase. Therefore, the transformation from $Ni(OH)_2$ to NiOOH caused surface reconstruction triggered by the Ni oxidation reaction.

We found that this oxyhydroxide phase formation was reconstructed further during the OER and was reversible depending on the applied potential: this has not been reported in previous studies on LNO. This reversible change in topography and surface height was also obtained after multiple CV experiments (Fig. S2 in ESI†). As proposed by Bode *et al.*,[50] the conversion from β- to γ-NiOOH occurs during overcharging, thereby causing a significant increase in the inter-slab distance from ~4.8 Å to ~7 Å. This change in height is believed to be caused by an intercalation of alkali cations[51] with a deprotonated γ-NiOOH intermediate during the OER.[52,53] Further reconstruction was observed that corresponded to a marked increase in the height of surface particles under a rapid OER, which may have contributed to this reported conversion of NiOOH. During discharging, γ-NiOOH could be reduced to β-$Ni(OH)_2$, with a decrease in inter-slab spacing to 4.6 Å. Similarly, a reduction and disappearance of higher particles was observed during this reduction process. Thus, the consistency of our data with that of previous studies suggested that the reversible reconstruction of topography was likely related to transformation of the $Ni(OH)_2$/NiOOH redox reaction: this is shown schematically in Fig. 5. Considering that the height difference between $Ni(OH)_2$ and γ-NiOOH in Fig. 5 was ~0.24 nm, a change in surface height of ~2 nm in EC-STM during the OER (Fig. 2h) corresponded to about eight layers of Ni (oxy)hydroxide. This Ni-containing layer following the OER could also be visible by *ex situ* ARXPS. The

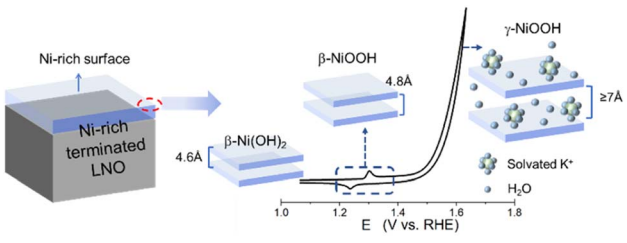

Fig. 5 Potential-dependent surface $Ni(OH)_2$/NiOOH redox transition of LNO (schematic). The transformation of $Ni(OH)_2$/NiOOH is illustrated using the top two layers on a Ni-rich surface as an example.

ratio of La 4d/Ni 3p decreased from 4.51 to 3.83 during the OER for Ni-rich terminated LNO according to surface-sensitive ARXPS (Fig. 2b and S7†). This change in the ratio indicated a small increase in thickness of the Ni-rich layer after the OER, which was not consistent with the results of eight layers of Ni (oxy)hydroxide based on Fig. 5. Thus, the model of $Ni(OH)_2$/NiOOH redox transformation could explain the dynamic reconstruction observed by EC-STM qualitatively, but could not match it closely quantitatively, which should be explored further in future work. Also, due to the limited chemical resolution of STM, precise determination of the chemical information of the observed structure and different types of NiOOH from STM images was difficult, which requires further *in situ* characterization to provide more detailed information.

Conclusions

We directly observe the surface reconstruction of a single-crystal LNO film at the atomic level during the OER using EC-STM. Combining quantitative analyses of STM images by mean height and height histograms, we demonstrated that the structural dynamics of surface changes as a function of the electrode potential were reversible. This structural reconstruction of LNO film was correlated directly with Ni-related species by manipulation of the components of LNO termination. Furthermore, based on previous reports, the reversible surface reconstruction could be induced by $Ni(OH)_2$/NiOOH redox transformation on the LNO surface. Our findings open-up new opportunities to unravel the connection between the local structure and interfacial reaction of well-defined single-crystal films under electrochemical conditions. Our data provide a promising pathway for fundamental mechanistic OER studies and future exploitation of electrocatalysts.

Data availability

Data are available from the corresponding authors upon request.

Author contributions

K. H.-L. Z., J. C., J.-W. Y., and Y. S. conceived and designed the project. K. H.-L. Z., J. C., and J.-W. Y. supervised the experiments. Y. S. carried out the EC-STM and AFM experiments. C.-R. W. prepared the single-crystal samples and carried out XRD spectroscopy. Y. S. and C.-R. W. carried out the CV experiment and XPS experiment. All authors analysed the results and co-wrote the manuscript.

Conflicts of interest

There are no conflicts of interest to declare.

Acknowledgements

We acknowledge funding support by the National Natural Science Foundation of China (21991151, 21991150, 21861132015, 22021001, 92161113, 91945301 and 22072123) and Xiamen Science and Technology Plan Project (3502Z20203027). We thank Y.B. Zhuang for help with writing the discussion section of this manuscript.

References

1 S. Anantharaj, S. R. Ede, K. Sakthikumar, K. Karthick, S. Mishra and S. Kundu, *ACS Catal.*, 2016, **6**, 8069–8097.
2 Z. W. Seh, J. Kibsgaard, C. F. Dickens, I. Chorkendorff, J. K. Nørskov and T. F. Jaramillo, *Science*, 2017, **355**, eaad4998.
3 Z. P. Ifkovits, J. M. Evans, M. C. Meier, K. M. Papadantonakis and N. S. Lewis, *Energy Environ. Sci.*, 2021, **14**, 4740–4759.
4 S. Haschke, M. Mader, S. Schlicht, A. M. Roberts, A. M. Angeles-Boza, J. A. Barth and J. Bachmann, *Nat. Commun.*, 2018, **9**, 1–8.
5 W. T. Hong, M. Risch, K. A. Stoerzinger, A. Grimaud, J. Suntivich and Y. Shao-Horn, *Energy Environ. Sci.*, 2015, **8**, 1404–1427.
6 M. S. Burke, L. J. Enman, A. S. Batchellor, S. Zou and S. W. Boettcher, *Chem. Mater.*, 2015, **27**, 7549–7558.
7 L. Han, S. Dong and E. Wang, *Adv. Mater.*, 2016, **28**, 9266–9291.
8 J. Y. Zhang, W. W. Li, R. L. Z. Hoye, J. L. MacManus-Driscoll, M. Budde, O. Bierwagen, L. Wang, Y. Du, M. J. Wahila, L. F. J. Piper, T.-L. Lee, H. J. Edwards, V. R. Dhanak and K. H. L. Zhang, *J. Mater. Chem. C*, 2018, **6**, 2275–2282.
9 L. Wang, K. A Stoerzinger, L. Chang, X. Yin, Y. Li, C. S. Tang, E. Jia, M. E. Bowden, Z. Yang, A. Abdelsamie, L. You, R. Guo, J. Chen, A. Rusydi, J. Wang, S. A. Chambers and Y. Du, *ACS Appl. Mater. Interfaces*, 2019, **11**, 12941–12947.
10 L. Wang, Z. Yang, M. Bowden, J. Freeland, S. Peter, S. Spurgeon, B. Matthews, W. Samarakoon, H. Zhou, Z. Feng, M. Engelhard, Y. Du and S. Chambers, Hole-Trapping-Induced Stabilization of Ni^{4+} in $SrNiO_3/LaFeO_3$ Superlattices, *Adv. Mater.*, 2020, **32**, 2005003.
11 T. Guo, L. Li and Z. Wang, *Adv. Energy Mater.*, 2022, **24**, 2200827.
12 X. Li, X. Su, Y. Pei, J. Liu, X. Zheng, K. Tang, G. Guan and X. Hao, *J. Mater. Chem. A*, 2019, **7**, 10745–10750.
13 H. J. Lee, S. Back, J. H. Lee, S. H. Choi, Y. Jung and J. W. Choi, *ACS Catal.*, 2019, **9**, 7099–7108.
14 G. Fu, W. Li, J.-Y. Zhang, M. Li, C. Li, N. Li, Q. He, S. Xi, D. Qi, J. L. MacManus-Driscoll, J. Cheng and K. H. Zhang, *Small*, 2021, **17**, 2006930.
15 J. Li, D. Chu, H. Dong, D. R. Baker and R. Jiang, *J. Am. Chem. Soc.*, 2019, **142**, 50–54.
16 S. R. Ede and Z. Luo, *J. Mater. Chem. A*, 2021, **9**, 20131–20163.
17 S. R. Ede, C. N. Collins, C. D. Posada, G. George, H. Wu, W. D. Ratcliff, Y. Lin, J. Wen, S. Han and Z. Luo, *ACS Catal.*, 2021, **11**, 4327–4337.
18 J. Wang, S.-J. Kim, J. Liu, Y. Gao, S. Choi, J. Han, H. Shin, S. Jo, J. Kim, F. Ciucci, H. Kim, Q. Li, W. Yang, X. Long, S. Yang, S.-P. Cho, K. H. Chae, M. G. Kim, H. Kim and J. Lim, *Nat. Catal.*, 2021, **4**, 212–222.

19 B.-J. Kim, E. Fabbri, M. Borlaf, D. F. Abbott, I. E. Castelli, M. Nachtegaal, T. Graule and T. J. Schmidt, *Mater. Adv.*, 2021, **2**, 345–355.
20 G. Solomon, A. Landström, R. Mazzaro, M. Jugovac, P. Moras, E. Cattaruzza, V. Morandi, I. Concina and A. Vomiero, *Adv. Energy Mater.*, 2021, **11**, 2170128.
21 X. Sun, X. Zhang, Y. Li, Y. Xu, H. Su, W. Che, J. He, H. Zhang, M. Liu, W. Zhou, W. Cheng and Q. Liu, *Small Methods*, 2021, **5**, 2100573.
22 J. Du, S. You, X. Li, B. Tang, B. Jiang, Y. Yu, Z. Cai, N. Ren and J. Zou, *ACS Appl. Mater. Interfaces*, 2019, **12**, 686–697.
23 S. Lee, A. Moysiadou, Y.-C. Chu, H. M. Chen and X. Hu, *Energy Environ. Sci.*, 2022, **15**, 206–214.
24 H. Mistry, A. S. Varela, S. Kühl, P. Strasser and B. R. Cuenya, *Nat. Rev. Mater.*, 2016, **1**, 1–14.
25 C. Wei, S. Sun, D. Mandler, X. Wang, S. Z. Qiao and Z. J. Xu, *Chem. Soc. Rev.*, 2019, **48**, 2518–2534.
26 S. Farokhipoor, C. Magén, S. Venkatesan, J. Íñiguez, C. J. Daumont, D. Rubi, E. Snoeck, M. Mostovoy, C. de Graaf, A. Müller, M. Döblinger, C. Scheu and B. Noheda, *Nature*, 2014, **515**, 379–383.
27 S. Prakash, S. Ghosh, A. Patra, M. Annamalai, M. R. Motapothula, S. Sarkar, S. J. Tan, J. Zhunan, K. P. Loh and T. Venkatesan, *Nanoscale*, 2018, **10**, 3356–3361.
28 H.-Y. Wang, Y.-Y. Hsu, R. Chen, T.-S. Chan, H. M. Chen and B. Liu, *Adv. Energy Mater.*, 2015, **5**, 1500091.
29 A. S. Raman, R. Patel and A. Vojvodic, *Faraday Discuss.*, 2021, **229**, 75–88.
30 W. Shen, J. Yin, J. Jin, Y. Hu, Y. Hou, J. Xiao, Y.-Q. Zhao and P. Xi, *Adv. Energy Sustainability Res.*, 2022, **8**, 2200036.
31 Y. Liang, J. H. Pfisterer, D. McLaughlin, C. Csoklich, L. Seidl, A. S. Bandarenka and O. Schneider, *Small Methods*, 2019, **3**, 1800387.
32 H. Feng, X. Xu, Y. Du and S. X. Dou, *Electrochem. Energy Rev.*, 2021, **4**, 249–268.
33 C. Stumm, M. Bertram, M. Kastenmeier, F. D. Speck, Z. Sun, J. Rodríguez-Fernandez, J. V. Lauritsen, K. J. Mayrhofer, S. Cherevko, O. Brummel and J. Libuda, *Adv. Funct. Mater.*, 2021, **31**, 2009923.
34 J. Hwang, R. R. Rao, L. Giordano, Y. Katayama, Y. Yu and Y. Shao-Horn, *Science*, 2017, **358**, 751–756.
35 J. Liu, E. Jia, L. Wang, K. A. Stoerzinger, H. Zhou, C. S. Tang, X. Yin, X. He, E. Bousquet, M. E. Bowden, A. T. S. Wee, S. A. Chambers and Y. Du, *Adv. Sci.*, 2019, **6**, 1901073.
36 L. Chang, L. Wang, L. You, Z. Yang, A. Abdelsamie, Q. Zhang, Y. Zhou, L. Gu, S. A Chambers and J. Wang, *ACS Appl. Mater. Interfaces*, 2019, **11**, 16191–16197.
37 O. Q. Carvalho, P. Adiga, L. Wang, J. Liu, E. Jia, Y. Du, S. Nemšák and K. A. Stoerzinger, *J. Phys. D: Appl. Phys.*, 2021, **54**, 274003.
38 L. Wang, P. Adiga, J. Zhao, W. S. Samarakoon, K. A. Stoerzinger, S. R. Spurgeon, B. E. Matthews, M. E. Bowden, P. V. Sushko, T. C. Kaspar, G. E. Sterbinsky, S. M. Heald, H. Wang, L. W. Wangoh, J. Wu, E.-J. Guo, H. Qian, J. Wang, T. Varga, S. Thevuthasan, Z. Feng, W. Yang, Y. Du and S. A. Chambers, *Nano Lett.*, 2021, **21**, 8324–8331.
39 P. Adiga, L. Wang, C. Wong, B. E. Matthews, M. E. Bowden, S. R. Spurgeon, G. E. Sterbinsky, M. Blum, M.-J. Choi, J. Tao, T. C. Kaspar, S. A. Chambers, K. A. Stoerzinger and Y. Du, *Nanoscale*, 2023, **15**, 1119–1127.
40 J. Liu, E. Jia, K. A. Stoerzinger, L. Wang, Y. Wang, Z. Yang, D. Shen, M. H. Engelhard, M. E. Bowden, Z. Zhu, S. A. Chambers and Y. Du, *J. Phys. Chem. C*, 2020, **124**, 15386–15390.
41 C. Baeumer, J. Li, Q. Lu, A. Y.-L. Liang, L. Jin, H. P. Martins, T. Duchoň, M. Glöß, S. M. Gericke, M. A. Wohlgemuth, M. Giesen, E. E. Penn, R. Dittmann, F. Gunkel, R. Waser, M. Bajdich, S. Nemšák, J. T. Mefford and W. C. Chueh, *Nat. Mater.*, 2021, **20**, 674–682.
42 M. Zier, S. Oswald, R. Reiche and K. Wetzig, *Appl. Surf. Sci.*, 2005, **252**, 234–239.
43 L. Qiao and X. Bi, *Europhys. Lett.*, 2011, **93**, 57002.
44 J. Deng, M. R. Nellist, M. B. Stevens, C. Dette, Y. Wang and S. W. Boettcher, *Nano Lett.*, 2017, **17**, 6922–6926.
45 J. O. M. Bockris and T. Otagawa, *J. Electrochem. Soc.*, 1984, **131**, 290.
46 O. Q. Carvalho, P. Adiga, L. Wang, J. Liu, E. Jia, Y. Du, S. Nemšák and K. A. Stoerzinger, *J. Phys. D: Appl. Phys.*, 2021, **54**, 274003.
47 L. F. Huang, M. J. Hutchison, R. J. Santucci Jr, J. R. Scully and J. M. Rondinelli, *J. Phys. Chem. C*, 2017, **121**, 9782–9789.
48 Y. Liang, S. Parreiras, S. Lee, K. Banjac, V. Boureau, J. M. Gallego, X. Hu, D. Écija, and M. Lingenfelder, *Operando nanoscale imaging reveals Fe doping of Ni oxide enhancing oxygen evolution reaction via fragmentation and formation of dual active sites*, 2022, DOI: **10.21203/rs.3.rs-1501975/v1**.
49 Y. Sun, R. Li, X. Chen, J. Wu, Y. Xie, X. Wang, K. Ma, L. Wang, Z. Zhang, Q. Liao, Z. Kang and Y. Zhang, *Adv. Energy Mater.*, 2021, **11**, 2003755.
50 H. Bode, K. Dehmelt and J. Witte, *Electrochim. Acta*, 1966, **11**, 1079–1087.
51 S.-L. Pyun, K.-H. Kim and J.-N. Han, *J. Power Sources*, 2000, **91**, 92–98.
52 O. Diaz-Morales, I. Ledezma-Yanez, M. T. Koper and F. Calle-Vallejo, *ACS Catal.*, 2015, **5**, 5380–5387.
53 O. Diaz-Morales, D. Ferrus-Suspedra and M. T. Koper, *Chem. Sci.*, 2016, **7**, 2639–2645.